

Effect of the nitrogen/carbon ratio in the organic ligand of a nickel single-atom catalyst on its electrochemical activity in CO₂ reduction

Hyeonuk Choi ^{a,1}, Min Gwan Ha ^{b,1}, Jungwon Suh ^a, Chulwan Lim ^b, Beomil Kim ^a, Sun Eon Wang ^a, Jang Yong Lee ^c, Hyung-Suk Oh ^{b,d,*}, Jihun Oh ^{a,**}

^a Department of Materials Science and Engineering, Korea Advanced Institute of Science and Technology (KAIST), 291 Daehak-ro, Yuseong-gu, Daejeon 34141, the Republic of Korea

^b Clean Energy Research Center, Korea Institute of Science and Technology (KIST), Hwarang-ro 14-gil 5, Seongbuk-gu, Seoul 02792, the Republic of Korea

^c Hydrogen Energy Research Center, Korea Research Institute of Chemical Technology (KRICT), Daejeon 34114, the Republic of Korea

^d KIST-SKKU Carbon-Neutral Research Center, Sungkyunkwan University (SKKU), Suwon, 16419, the Republic of Korea



ARTICLE INFO

Keywords:

Single-atom catalyst
Small organic ligands
Electrochemical CO₂ reduction
Large-scale synthesis
CO production

ABSTRACT

Simple, large-scale synthesis of metal single-atom catalysts (SACs) is limited by the aggregation of metal atoms on the support material surface. The N atoms in small organic ligands (SOLs) can anchor single metal atoms, affording abundant surface-active sites. In this study, we investigated the effect of the nitrogen/carbon ratio (N/C) in SOLs on the properties of the resultant Ni single-atom confined nitrogen-doped carbon black (Ni-NCB). The N/C ratio affected the thermal stability of Ni-NCB_N/Cs during carbonization, and the optimal Ni-NCB (Ni-NCB_0.5) was synthesized with the SOL 2-methylimidazole. Ni-NCB_0.5 achieved a CO partial current density of > 500 mA cm⁻² and high CO Faradaic efficiency (96.4 %) in the CO₂ reduction reaction. The 3- and 4-cell stack systems with Ni-NCB_0.5 (25 cm² area per unit cell) exhibited an overall current of 10 A, high CO selectivity (> 96.0 %), and long-term stability (50 h). This synthetic strategy for SACs can be commercialized and even extended to other industrial electrocatalysts.

1. Introduction

The electrochemical conversion of CO₂ into high-value products is a key approach for achieving global carbon neutrality. To commercialize this approach, efficient electrocatalysts with high product selectivity, low overpotential, and high stability and scalability are required. CO₂ conversion electrocatalysts with noble metals such as Au and Ag suffer from competing reactions such as the hydrogen evolution reaction and high production costs. To address these issues, single-atom catalysts (SACs) with individual metal atoms dispersed on heterogeneous substrates have been developed [1,2]. SACs exhibit maximum atomic efficiency and high selectivity due to the uniform dispersion of their active sites [3]. Furthermore, transition metals (e.g., Ni and Co), which previously could not be used in CO₂ conversion due to their strong CO adsorption energy, can be used for CO₂ conversion after appropriate electronic structure control, which also provides a cost advantage. To

date, many methods have been reported for the synthesis of carbon-based transition-metal SACs. However, the high surface energy of single atoms at the atomic level requires complex procedures or the use of expensive organic ligands for atom-level control. Therefore, a simple and cost-effective strategy for synthesizing SACs using readily available precursors must be developed.

Coordinative pyrolysis, in which a metal precursor is annealed with a coordination precursor, is an effective method for introducing coordination into the supporting materials of SACs [4]. Considering the scalability of this straightforward method, researchers have explored various organic ligands as nitrogen (N)-containing precursors for synthesizing efficient SACs [5–9]. Notably, complex organic precursors such as porphyrins and metal-organic frameworks (MOFs) afford abundant anchoring sites and incorporate single-atom metals through adsorption, coordination, or ion exchange processes [10,11]. Additionally, the diverse N sites within MOFs stabilize metal atoms even at high

* Corresponding author at: Clean Energy Research Center, Korea Institute of Science and Technology (KIST), Hwarang-ro 14-gil 5, Seongbuk-gu, Seoul 02792, the Republic of Korea.

** Corresponding author.

E-mail addresses: hyung-suk.oh@kist.re.kr (H.-S. Oh), jihun.oh@kaist.ac.kr (J. Oh).

¹ H.C and M.G.H. are equally contributed.

temperatures, forming strong M—N bonds and affording atomically dispersed metal sites in the resulting SACs. However, pyrolysis of MOF-based templates is limited by low yields, the necessity of expensive organic linkers and complex pretreatment, and fixed N content. The use of N-containing small organic ligands (SOLs) on a carbon-based support is an attractive alternative method to solve above synthesis limitation [5,6,8]. This approach bypasses the complicated step of preparing complex organic molecules, offering a more scalable and reasonable pathway for the synthesis of SACs. Even though various SOLs have been used for synthesizing SACs, the effects of SOLs on the formation of atomic active sites have not yet been investigated.

The high surface energy of atomically dispersed metal atoms is challenging due to the aggregation of metal atoms during synthesis, which decreases the availability of single-atom catalytic active sites. Therefore, controlling the coordination element is imperative to achieve an optimal electronegativity difference between nitrogen and the metal atom and to anchor the metal atoms [12]. Nitrogen exhibits strong coordination bonding with transition metals and stabilizes over 20 single-atom metal species, thus influencing the electronic properties of metals and preventing their rapid agglomeration into clusters [13–16]. Therefore, nitrogen is the most commonly used coordination element in SACs, and regulating the nitrogen content in the supporting material is crucial for achieving abundant atomic active sites on SACs. In this context, we aimed to investigate the effect of the nitrogen-to-carbon (N/C) ratio in the SOL on the amount of nitrogen defects in the carbon matrix, which determines the number of atomic active sites in the SACs.

In this study, we synthesized Ni single-atom confined nitrogen-doped carbon blacks (Ni-NCBs) using SOLs with a wide range of N/C ratios (0.17–2.00) to control the amount of N content in the supporting material and to obtain abundant atomic active sites. Through testing SOLs with various N/C ratios, we have identified three main findings: (1) morphological and surface area variations depend on the N/C ratio, (2) a significant correlation exists between the N and Ni content in Ni-NCBs, (3) the proper N/C ratio range is influenced by the varying thermal stability of SOLs. The optimal N/C ratio was identified, and the electrocatalytic properties of the Ni-NCB prepared using this optimal ratio were evaluated in an electrochemical CO₂ reduction reaction (CO₂RR). Furthermore, the electrochemical performance of a cell stack of the optimal Ni-NCB was evaluated for potential commercialization. Therefore, our results demonstrate that a deep understanding of precursors is critical for synthesizing efficient SACs.

2. Experimental section

2.1. Synthesis of Ni-NCB_N/C ratio

Carbon black (CB; 400 mg), 3.3 mM of small organic ligands (SOLs) (1,10-phenanthroline (Phen), o-phenylenediamine (oPD), 2-methylimidazole (2-MeIm), adenine, and melamine for Ni-NCB_0.17, 0.33, 0.5, 1, and 2, respectively), 0.825 mM of Ni(NO₃)₂·6H₂O, and 200 mL of ethanol (for Phen, oPD, and 2-MeIm) or deionized water (for adenine and melamine) were added to a 500 mL round-bottom flask. This mixture was ultrasonicated for 20 min for homogeneous dispersion. The selection of the solvent (ethanol or water) depended on the solubility of the SOL. The solution ethanol solvent was evaporated in a rotavap (250 rpm and 65 °C) and ground into a fine powder using a mortar and pestle. The powder was calcined in a tube furnace at 800 °C at a heating rate of 5 °C min⁻¹ for 2 h under an Ar flow of 500 mL min⁻¹. The calcined powder was cooled and further ground into a fine powder using a mortar and pestle.

2.2. Synthesis of Ni single-atom confined nitrogen-doped carbon (Ni-NC)_{N/C} samples

The preparation of Ni-NC_N/C samples was similar as Ni-NCB_N/C

excepting adding carbon black.

2.3. Synthesis of Ni-NCB_1:# samples

The preparation of Ni-NCB_1:# samples was similar as Ni-NCB_0.5 (2-MeIm) except using different amount of 2-MeIm. The x mM of 2-MeIm was changed as 3.3, 6.6, 13.2, 26.4, and 52.8 mM for Ni-NCB_1:4, 1:8, 1:16, 1:32, and 1:64.

2.4. Large-scale synthesis of Ni-NCB using the optimal SOL (2-MeIm, N/C = 0.5)

CB (8 g), 21.6 g of 2-MeIm, 4.8 g of Ni(NO₃)₂·6H₂O, and 2 L of ethanol were added to a glass bottle (2 L) and ultrasonicated for 1 h for homogeneous dispersion. The solution was rotated at 250 rpm and heated at 65 °C in a vacuum state using a rotary evaporator for ethanol evaporation. The dried powder was ground using a mortar and pestle. The ground powder was calcinated at 800 °C (5 °C min⁻¹ of increasing temperate rate) in a tube furnace for 2 h under 500 mL min⁻¹ of argon flow condition. After cooling, the calcinated powder was ground using a mortar and pestle.

2.5. Preparation of catalyst-loaded gas diffusion electrodes

Ni-NCB gas diffusion electrodes were fabricated by spray-coating the catalyst ink on the microporous layer side of a commercially available carbon paper (Sigracet GDL-39BB, Fuel Cell Store, Texas, USA). To prepare the catalyst ink, a solution of 40 mg of the catalyst, 20 mL of ethanol, and 48.2 μL of a 5 wt% Nafion solution was ultrasonicated for 30 min. The resulting catalyst ink was spray-coated on carbon paper placed on a hotplate at 80 °C using s to achieve a total catalyst loading of 1.0 mg cm⁻².

2.6. Electroreduction of CO₂ in a gas diffusion flow electrolyzer

A gas diffusion electrode (GDE)-based flow cell was constructed with a 3-electrode system. The flow cell consisted of cathode and anode chambers separated by an anion-exchange membrane (Sustainion membrane, Dioxide Materials, Florida, USA). A Hg/HgO (1 M NaOH) electrode and a NiFeMo foil (Alfa Aesar) were used as the reference electrode and anode, respectively. The working and counter electrodes had areas of 1 cm² and 2 cm², respectively. The catalyst loading used for the Ni-NCB cathodes was 0.8 mg cm⁻². During the electrochemical measurements, a 1.0 M KOH electrolyte was continuously circulated from a 100 mL electrolyte reservoir using a peristaltic pump (Masterflex, Gelsenkirchen, Germany) at a flow rate of 10 mL min⁻¹. The flow rate of CO₂ gas to the cathode gas chamber was 20 sccm and was controlled by a mass flow controller (MFC KOREA, Incheon, ROK). The anode compartment was filled with 10 mL of 1 M KOH electrolyte.

Chronopotentiometry (CP) was performed using an electrochemical potentiostat (Biologic, Grenoble, France). Prior to each electrochemical measurement, an activation step was conducted at a current density of 10 mA cm⁻² for 10 min. The CP measurements were acquired for 20 min for each CO₂ reduction experiment. During the measurements, the solution ohmic resistance was determined by electrochemical impedance spectroscopy. The ohmic drop was manually compensated (100 % iR correction) at each CP step. The applied electrode potential (Hg/HgO) was converted to the reversible hydrogen electrode (RHE) scale using the following equation:

$$E_{RHE} = E_{Hg/HgO} + 0.0591 * pH + E_{Hg/HgO}^0$$

where the E_{Hg/HgO}⁰ is 0.098 V vs NHE; pH of the 1 M KOH solution is 14.

The gaseous products were quantified using an on-line gas chromatograph (GC; 6500GC System, YOUNG IN Chromass, Anyang, ROK) equipped with a thermal conductivity detector (TCD). The Faradaic ef-

ficiencies (FE) of the products, CO and H₂, were calculated using the following equation:

$$FE_{product} (\%) = \frac{n_{product} * z_{product} * F}{Q} \times 100$$

where $n_{product}$ is number of moles of the product, which was calculated based on the flow rate of the outlet gas, measured using an electronic gas flow meter; $z_{product}$ is the stoichiometric number of the electrons required for producing the product (2 for CO and H₂); F is Faraday's constant (96,485 C mol⁻¹); and Q is the amount of charge passed during the electrolysis. The partial current density of each product ($j_{product}$) was determined by multiplying the $FE_{product}$ with the applied total current density (j_{total}).

The Nyquist plots were obtained via electrochemical impedance spectroscopy (EIS) at an applied cathodic potential of -1.10 V vs Hg/HgO, which is negligibly affected by mass transfer. The CO₂ supply rate and catholyte flow rate were maintained at 20 sccm and 10 m L min⁻¹, respectively. Scans were performed using 100 different frequencies, from 10 kHz to 100 mHz. The measured data were fitted using a simplified Randles circuit without the Warburg element. The diameter of the semi-circle in the Nyquist plot represents the charge transfer resistance (R_{ct}) in the CO₂RR, while the x-intercept at high frequency represents the electrolyte resistance.

2.7. Electroreduction of CO₂ in unit- and stack-type membrane electrode assembly

A membrane electrode assembly (MEA) was used in this study [17]. The active area of the MEA-based electrode was 25 cm², with a manufactured electrode and IrO₂/Pt/Ti mesh (Commercial IrO₂) was sprayed on the anode Pt-coated Ti mesh; 0.25 mg cm⁻² per layer, targeting a total of 1 mg cm⁻²) as the cathode and anode, respectively. A custom-made anion exchange membrane (QPC-TMA membrane, 25 cm²) was used [18]. Serpentine-shaped channels were used on the anode and cathode sides. Humidified CO₂ at 80 °C, which is the reactant gas, was introduced into the cathodic inlet at a flow rate of 200 sccm. The electrolyte (0.1 M KHCO₃) was circulated to the anode via a pump. For the 3- and 4-stack systems, stack-type electrolyzers were constructed by connecting unit cells in series to each bipolar plate, with an active area of 25 cm². Pt-coated Ti serpentine-type and Au-coated Ti serpentine-type flow plates were used as the anode and cathode, respectively. Humidified CO₂ was supplied to the cathode at a flow rate of 1000 sccm. The cathode and anode in the unit cell were similar to those used in the stack experiments. A VSP potentiostat (VMP3B-10, BioLogic) was used for electrochemical experiments.

The full cell energy efficiencies of unit and stack cell for CO formation (EE_{CO}) were calculated as follow:

$$EE_{CO} \text{ for unit cell } (\%) = \frac{1.34}{E_{unit \ cell}} \times FE_{CO}$$

$$EE_{CO} \text{ for stack cell } (\%) = \frac{1.34 \times n_{stack}}{E_{stack \ cell}} \times FE_{CO}$$

where 1.34 V is the thermodynamic potential between the reduction potential of CO₂ to CO and the oxidation potential of H₂O to O₂, n_{stack} is the number of stacks, and $E_{stack \ cell}$ is the applied potential of the stack cell.

The single-pass conversion (SPC) of CO₂ to CO was determined using the following equation:

$$SPC \ (\%) = \frac{n_{CO}}{n_{CO_2}} \times 100$$

where n_{CO} and n_{CO_2} is the number of moles of the CO produced and the CO₂ fed into the electrolyzer, respectively.

3. Results and discussion

3.1. Synthesis and characterization

Ni-NCBs were synthesized using a facile pyrolysis-based method, which is a mass-production approach for synthesizing SACs. In this method, the SOLs, carbon black supports, and Ni precursors are uniformly dispersed in a solvent. This solution is dried and heat-treated to afford a powder (Fig. 1a). Five SOLs, which are commonly used for preparing Ni-NCBs [1,10-phenanthroline (Phen), o-phenylenediamine (oPD), 2-methylimidazole (2-MeIm), adenine, and melamine], were selected for synthesizing Ni-NCBs using the N/C ratios of 0.17, 0.33, 0.5, 1, and 2 (Fig. 1b). The synthesized Ni-NCBs were denoted by Ni-NCB_N/C, where N/C is the N/C ratio of the used SOLs.

The morphology and the single-atom active sites of Ni-NCBs were characterized via scanning electron microscopy (SEM) and transmission electron microscopy (TEM). Their morphology depended on the N/C ratio of the organic ligand (Fig. 2a-e and S1). The lowest N/C ratio (0.17, Phen) afforded a nanosheet-like carbon matrix on carbon black (Fig. 2a and S1a), which is consistent with previous reports [19]. However, as the N/C ratio increased, the sheet-like structure collapsed, and from an N/C ratio of 0.5, carbon nanotubes began to grow and lengthen on the support material (Fig. 2c-e and S1c-e). A melamine-based carbon matrix exhibits nanotube-like morphology, owing to the conversion of melamine into carbon nitride at ~500 °C and the formation of carbon nanotubes at 800 °C [20,21]. The growth of carbon nanotubes is likely due to the organic ligand acting as the carbon source on Ni nanoparticles (NPs), which are formed due to uncoordinated Ni ion/atom aggregation during high-temperature treatment [22].

The atomic Ni active sites on the surface of the prepared Ni-NCBs were confirmed via high-angle annular dark-field scanning transmission electron microscopy (HAADF-STEM) imaging (Fig. 2f-j). Isolated Ni atoms were distinguishable in the carbon matrix due to their higher Z contrasts among Ni, N, and C. Regardless of the organic ligand used, all the samples exhibited well-dispersed Ni atoms on the carbon support materials. Energy dispersive X-ray spectroscopy (EDS) elemental mapping images confirmed the homogenous dispersion of Ni and N on the catalyst surface (Fig. 2k-o and S2). The co-produced Ni NPs were encapsulated in a carbon shell with thicknesses greater than several nanometers (Fig. S1). However, an even, three-layered carbon shell on Ni NPs would block the active site, limiting mass transfer and restricting the catalytic reaction [23]: the Ni NPs primarily exist in a carbon-encapsulated state even after subjecting them to strong acid leaching using 6 M HCl. HAADF-STEM and XRD results of the Ni-NCB after acid leaching are shown in Fig. S3a and b, respectively. Furthermore, even the Ni NPs are present without carbon shell on the support surface, well-known CO poisoning effect of Ni NPs can induce a negligible impact of Ni NPs on the CO₂RR [24].

Brunauer-Emmett-Teller (BET) analysis and Raman spectroscopy were performed to investigate the physicochemical properties of Ni-NCBs (Fig. S4 and S5, respectively). All Ni-NCB_N/Cs exhibited large surface areas (> 180 m² g⁻¹) owing to the presence of carbon black as the support material and a consistent pore size of ~3.8 nm. The Raman spectra of the Ni-NCB_N/C samples exhibited the characteristic D band (1350 cm⁻¹) of disordered carbon atoms and the G band (1590 cm⁻¹) of sp²-hybridized graphitic carbon atoms. The I_D/I_G values of all Ni-NCB_N/Cs were ~1, which indicates a high degree of graphitization with no significant distinctions [25–27]. Hence, the variation in the N/C ratio of the SOL had a negligible impact on the pore structure and graphitic degree of the fabricated carbon support materials.

The coordination environment of the Ni atoms in the Ni-NCB_N/Cs was investigated using extended X-ray absorption fine structure (EXAFS) analysis (Fig. 3). The Fourier-transform EXAFS (FT-EXAFS) spectra showed prominent peaks at ~2.07 Å and 1.43 Å (Fig. 3a), corresponding to Ni–Ni and Ni–N bond lengths, respectively. However, no peak corresponding to the Ni–O bonds (1.70 Å) was observed,

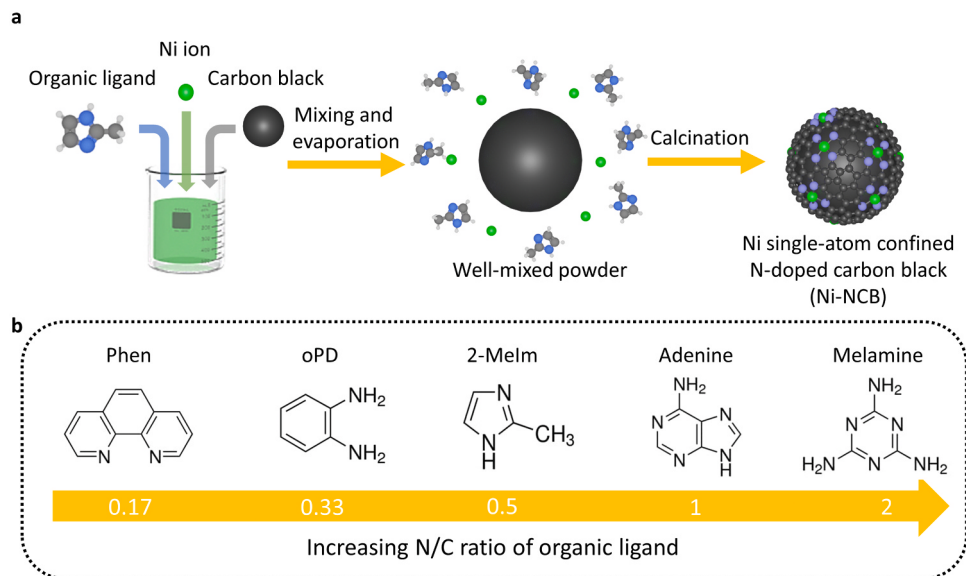


Fig. 1. Screening of optimal small organic ligands (SOLs) for the synthesis of efficient single-atom catalysts (SACs). (a) Synthesis of Ni single-atom confined nitrogen-doped carbon blacks (Ni-NCBs) using SOLs. (b) SOLs with different nitrogen/carbon (N/C) ratios.

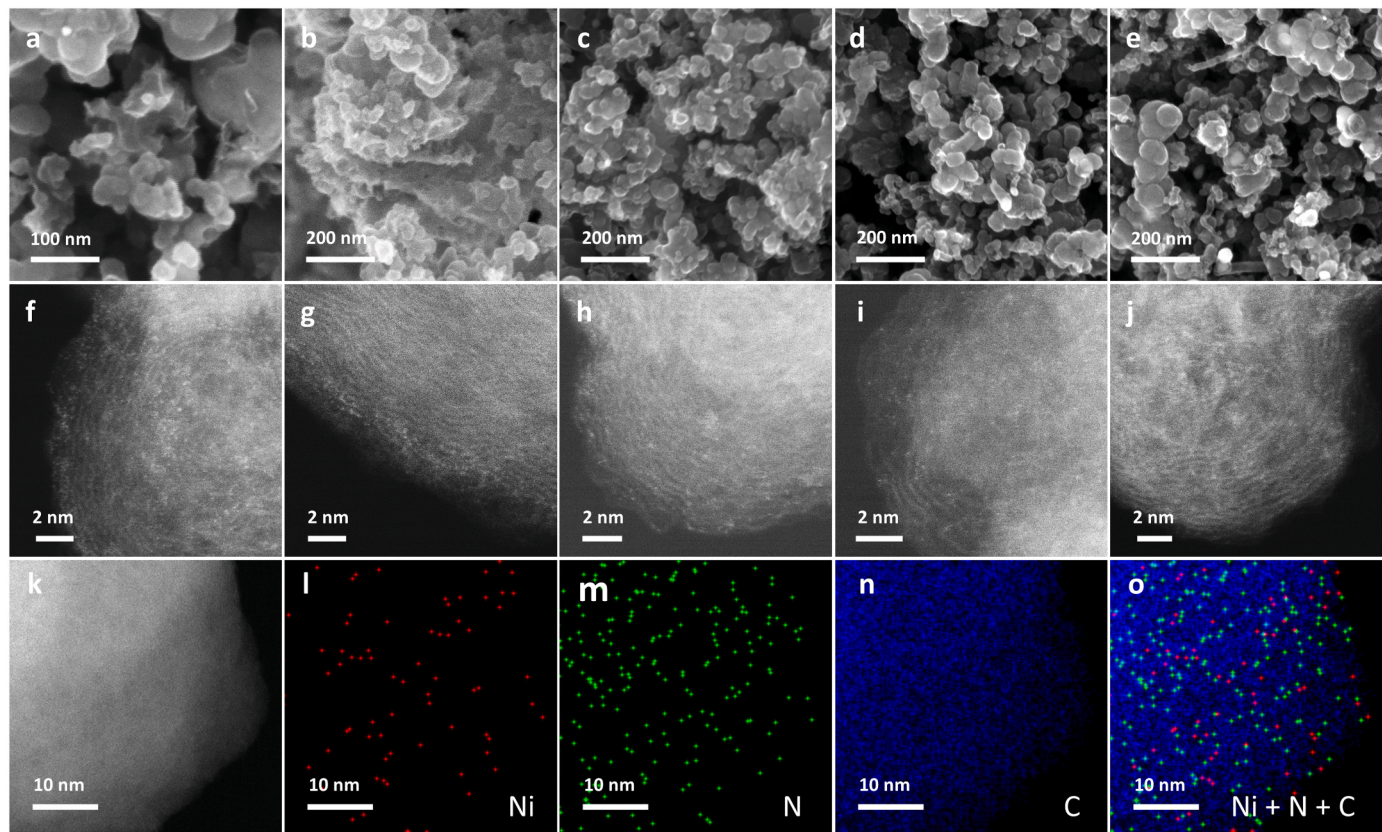


Fig. 2. Microscopic characterization of the Ni-NCBs synthesized from SOLs with different N/C ratios (Ni-NCB_{N/C}s). Scanning electron microscopy and high-angle annular dark-field scanning transmission electron microscopy (HAADF-STEM) images of (a and f) Ni-NCB_{0.17}, (b and g) 0.33, (c and h) 0.5, (d and i) 1, and (e and j) 2. (k) HAADF-STEM image of Ni-NCB_{0.17} and corresponding elemental mapping images of (l) Ni, (m) N, (n) C, and (o) all elements.

indicating that all Ni atoms were present as Ni—Ni and Ni—N bonds derived from Ni NPs and atomic Ni coordinated to N in the carbon support material, respectively. Furthermore, wavelet-transform EXAFS (WT-EXAFS) was used to determine the supplementary k -space (\AA^{-1}) to differentiate the backscattering atoms, even in cases where their peaks overlapped in the R -space (\AA). The maxima near 6.5 \AA^{-1} are associated

with the Ni-Ni bonds (Fig. S6), whereas the maxima at 5.5 \AA^{-1} suggest the co-existence of Ni NPs and atomic N [28]. Selected area electron diffraction (SAED) and powder X-ray diffraction (XRD) analysis of all Ni-NCB_{N/C}s confirmed the absence of nickel oxide (Fig. S1 and S7).

Bulk-scale analyses [elemental analysis (EA) and inductively coupled plasma (ICP) analysis] and surface-scale analysis [X-ray photoelectron

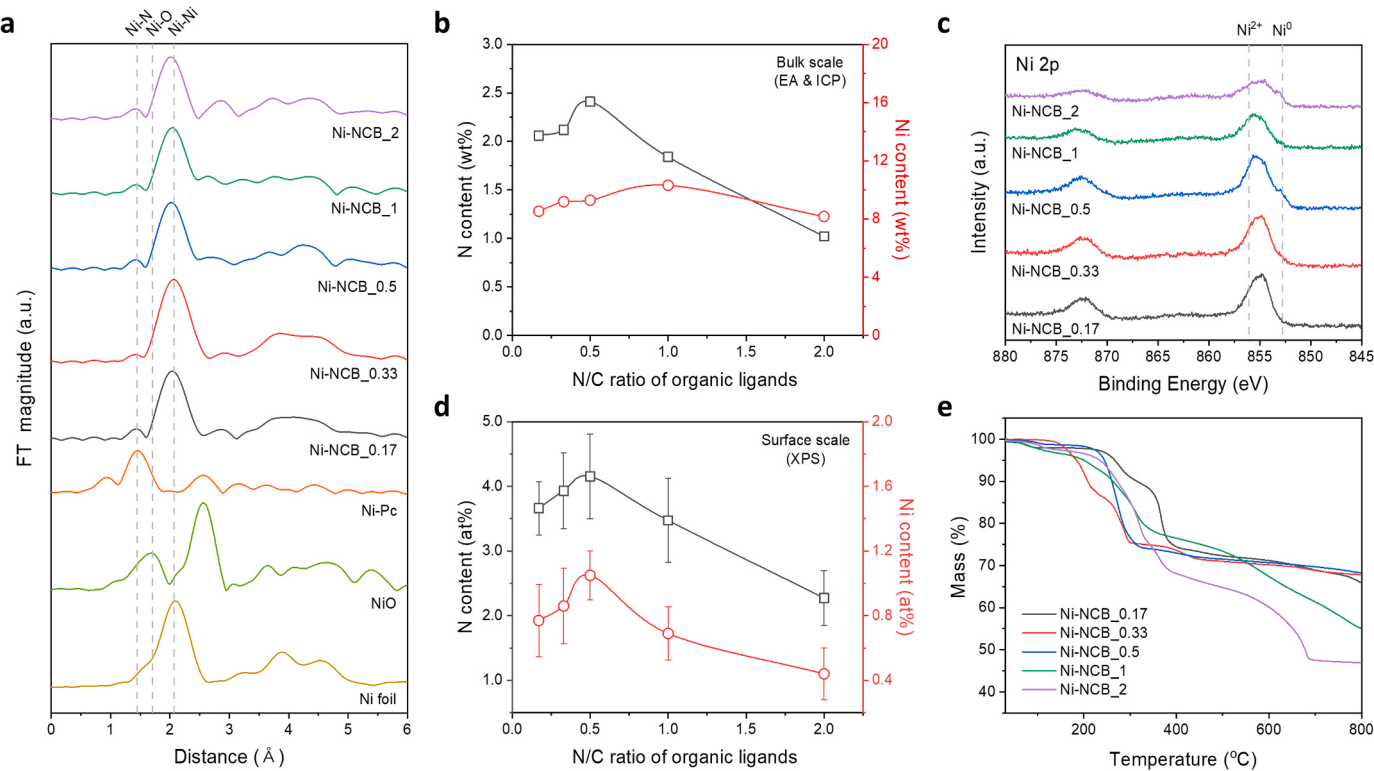


Fig. 3. Physicochemical characterization of Ni-NCB_N/Cs. (a) Fourier-transform K-edge extended X-ray absorption fine structure spectra of Ni-NCB_N/Cs and Ni-based reference materials. (b) N and Ni contents of Ni-NCB_N/Cs based on elemental analysis and inductively coupled plasma, respectively, for bulk scale analysis. (c) Ni 2p X-ray photoelectron spectra and (d) N and Ni contents of Ni-NCB_N/Cs. (e) Thermogravimetric analysis of Ni-NCB_N/Cs. When error bars are presented, data are represented as mean \pm standard deviation of at least 3 individual experiments.

spectroscopy (XPS)] were conducted to compare the composition of the Ni atoms in Ni-NCBs at the bulk and surface levels (Fig. 3b-d). EA and ICP analysis revealed that the bulk-scale N content increased with an increase in the N/C ratio of the organic ligand up to the peak at 0.5 and then decreased (Fig. 3b). Bulk-scale Ni content remained stable at ~ 9.1 wt% in all different organic ligands, implying that Ni NPs exist in the bulk level. However, the results of XPS are different from those of bulk-scale analyses [29]. The Ni 2p_{3/2} peak of Ni-NCB_N/C appeared at 855.4 ± 0.1 eV (Fig. 3c), which is consistent with that (855.4 eV) of Ni-NCB; this result is also in good agreement with the Ni-N pair in the reported EXAFS of Ni-NCBs, without the additional peaks of Ni(OH)₂ (855.7 eV), NiO₂ (853.6 eV), and metallic Ni (852.1 eV) [16]. These XPS results that our catalyst surface was constituted mostly by the Ni atomic active sites (i.e., Ni-N_x), whereas the Ni NPs were formed in the bulk. Moreover, the N 2s spectra of the Ni-NCB_N/Cs were deconvoluted into pyridinic N (398.8 eV), Ni-N (399.4 eV), pyrrolic N (400.3 eV), oxidized N (401.2 eV), and graphitic N (402.9 eV) (Fig. S8), indicating that N is well-coordinated with Ni. Additionally, the chemical state of N in Ni-NCB_N/C was nearly independent of the N/C ratio of the organic ligands, suggesting that the N/C ratio mainly influences the amount of doped N on the support material.

The XPS spectra confirmed that the trends of Ni and N contents on the catalyst surface are similar (Fig. 3d), indicating that N stabilizes Ni. This is consistent with a previous report, which revealed that the interaction of the localized p orbital of N with the d orbital of Ni stabilizes Ni [30]: controlling the number of heteroatoms in the carbon material could be a valuable approach to increasing the number of atomic active sites in SACs. An optimal N/C ratio of SOL was identified based on the fact that the Ni and N contents do not increase steadily but rather exhibits a peak depending on the N/C ratio of the organic ligand. Instead of the expected high amount of doped N following the thermal treatment of the SOL with the highest N/C ratio, we observed that the

highest N contents was observed at a ratio of 0.5 (Ni-NCB_0.5). Accordingly, Ni-NCB_0.5 showed highest single atomic Ni content of ~ 1 at% on the catalyst's surface.

Various organic ligands with excessively high N could be thermally polymerized between 400 and 600 °C to form carbon nitride, which has a relatively low thermal stability [31]. Considering that the N/C ratio of SOLs could be related to their thermal stability, we analyzed the catalyst precursor with various SOLs via thermogravimetric analysis (TGA) (Fig. 3e). The organic ligands with an N/C ratio exceeding 0.5 showed significant mass loss at > 500 °C and those with a higher N/C ratio showed a larger mass loss. In the latter case, intermediate structures with lower thermal stability are formed, resulting in a significant loss of N and C at 600 °C. This decreases the N content on the catalytic surface and lowers the yields of synthesis from 57.1 % to 42.6 % when SOLs with a higher N/C ratio are used (Fig. S9).

To further investigate the impact of calcination temperature on the formation of atomic Ni active sites, Ni-NCB samples prepared at 600 °C were analyzed using Raman, XRD, TEM, ICP, EA, XPS, and BET analyses. Raman analysis demonstrated that samples calcined at 600 °C exhibited both a higher I_D/I_G ratio, indicating less graphitization due to lower calcination temperature and more atomic active sites (Fig. S10). XRD analysis showed a reduction in Ni ion aggregation, leading to fewer Ni metal peaks compared to those processed at 800 °C. (Fig. S11). SEM and TEM analyses revealed similar morphological changes at both 600 °C and 800 °C (Fig. S12 and S13). Lower calcination temperatures resulted in the highest N content and surface area for samples with an N/C ratio of 1, a notable shift from the previous highest values observed in samples with an N/C ratio of 0.5. (Fig. S14). This observation suggests that the lower calcination temperature might have allowed organic ligands with higher N/C ratios, previously less heat-resistant, to stabilize and carbonize more effectively. These findings imply that optimal N/C ratios may vary depending on the synthesis temperature.

A summary of the effects of the N/C ratio of the organic ligands on the pyrolysis-based synthesis of Ni-NCBs is shown in Fig. 4. We confirmed that organic ligands with a low N/C ratio (< 0.5) stabilize the N atoms on the catalyst surface even at high temperatures. However, in this case, the N content after synthesis was slightly lower than that of an N/C ratio of 0.5. The use of organic ligands with an N/C ratio of 0.5 resulted in a large amount of N on the catalyst surface, which stabilizes Ni ions as single atoms, leading to a high number of single-atom active sites on the catalyst surface. In contrast, the use of organic ligands with an N/C ratio of > 0.5 resulted in a large amount of N loss during heat treatment due to thermal polymerization to generate intermediate structures that decomposed at higher temperatures due to low thermal stability. This leads to a significantly reduced N content on the catalyst surface and a relatively low number of single-atom active sites in the catalysts. Additionally, unreacted organic ligands act as carbon sources and form carbon shells or carbon nanotubes around Ni NPs on the catalyst surface. Hence, an optimal N/C ratio in the SOL plays a crucial role in the performance of the synthesized Ni-NCB.

Additionally, to investigate how carbon black influences the interaction between the organic ligands and Ni atoms, the Ni-NC samples, which are synthesized without adding carbon black, were prepared and analyzed by using SEM, TEM, XRD, and XPS. As depicted Fig. S15 and S16, SEM and TEM analyses indicate that a distinct variation in structure as the N/C ratio increased: starting with a flake-like carbon-based support at an N/C ratio of 0.17, progressively transitioning to more porous structures at N/C ratios of 0.33–0.5, and ultimately forming carbon nanotube supports at N/C ratios between 1 and 2. These microscopic results of Ni-NC samples are well-matched with them of Ni-NCB samples demonstrating N/C ratio can affect morphology change of carbon materials. Although the morphology differences between the samples became larger when carbon black was not added, the trend of morphology change with N/C ratio was consistent.

Moreover, XRD and XPS analyses suggest that carbon black helps avoid the clustering of Ni ions. The XRD patterns revealed weaker Ni crystal peaks in samples with carbon black, with estimated crystallite sizes of 43–59 nm compared to 200–338 nm in samples without carbon black (Fig. S17). This significant decrease in crystallite size of Ni nanoparticles indicates the dispersion effect of carbon black. Also, XPS analysis showed much reduced peaks of metallic Ni in samples with

carbon black, emphasizing its role in keeping Ni ions dispersed at the atomic level (Fig. S18). These results clearly demonstrate that adding carbon black as a conductive support not only improves the electrochemical properties of the catalysts but also effectively prevents Ni ion clustering, enabling the formation of atomic active sites.

3.2. Electrochemical CO_2 reduction reaction

As proof of concept, we compared the electrocatalytic activities and electrochemical properties of all the Ni-NCB_N/Cs in an electrochemical reduction of CO_2 to CO, which is a well-known electrocatalytic reaction of Ni-based single atom catalysts. A gas diffusion flow cell was used, and the catalysts were loaded on a carbon paper, which facilitates the feeding of sufficient CO_2 to avoid mass transfer limitation during CO_2RR (Fig. 5a). All Ni-NCB_N/Cs showed high CO_2RR performance (Fig. 5b and S19). However, Ni-NCB_N/Cs containing different numbers of active sites showed different overpotentials to reach the same CO partial current density (j_{CO}) (Fig. 5b). Ni-NCB_0.5, which has the highest number of active sites, required only 162 mV of overpotential to reach a total current density of 100 mA cm^{-2} , whereas Ni-NCB_2, which has the lowest number of active sites, required 314 mV of overpotential. However, all Ni-NCBs maintained a CO Faradaic efficiency of $> 95\%$ at 100 mA cm^{-2} and suppressed the hydrogen evolution reaction (HER) at -0.45 V vs RHE. This suggests that the difference between the overpotentials is associated with CO_2RR and not HER (Fig. 5c and S19).

Electrochemical surface area (ECSA) was evaluated via cyclic voltammetry. The ECSA values for Ni-NCB_0.17, Ni-NCB_0.33, Ni-NCB_0.5, Ni-NCB_1, and Ni-NCB_2 were 203.29, 222.1, 247.8, 242.1, and $216.45 \text{ m}^2 \text{ g}^{-1}$, respectively (Fig. 5d). The j_{CO} results were normalized with respect to their ECSA values (Fig. 5e), and the surface activity follows the order: Ni-NCB_0.5 > Ni-NCB_0.33 > Ni-NCB_0.17 > Ni-NCB_1 > Ni-NCB_2. To investigate the underlying factors responsible for the variation in the surface activity of Ni-NCB_N/Cs, we elucidated the relationship between the surface activity and the number of atomic Ni active sites. The j_{CO} values of Ni-NCB_N/Cs at -25 mV vs RHE were plotted against the Ni atomic percent on the catalyst surface (Fig. 5d). The ECSA-normalized j_{CO} values of Ni-NCB_N/Cs increased as the amount of the Ni active sites on the catalyst surface increased. This highlights the significance of controlling the N/C ratio of the SOL to

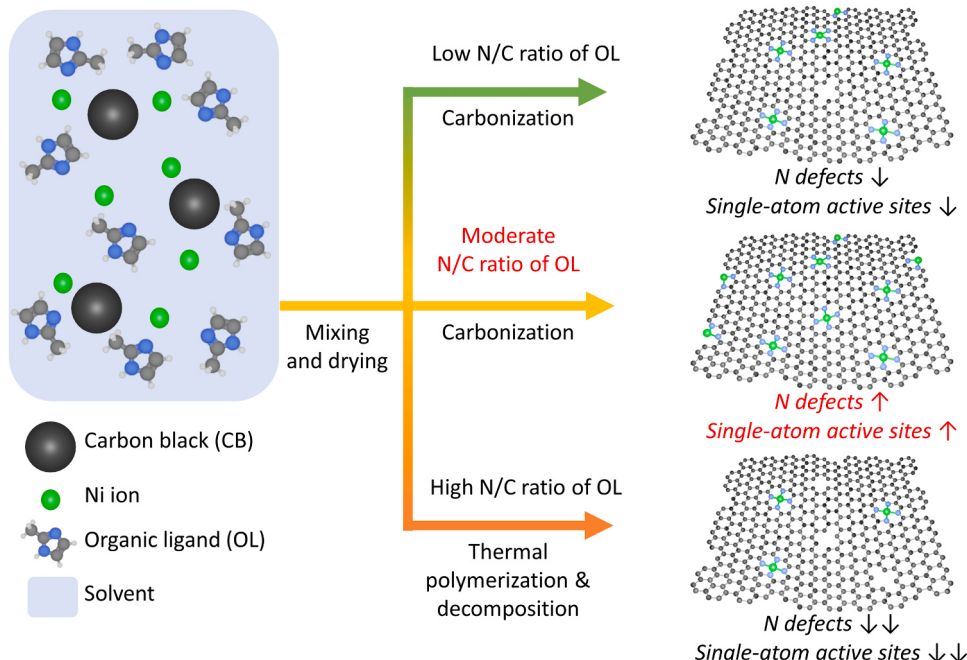


Fig. 4. Effects of the N/C ratios of SOLs on the properties of the synthesized Ni-NCB_N/Cs.

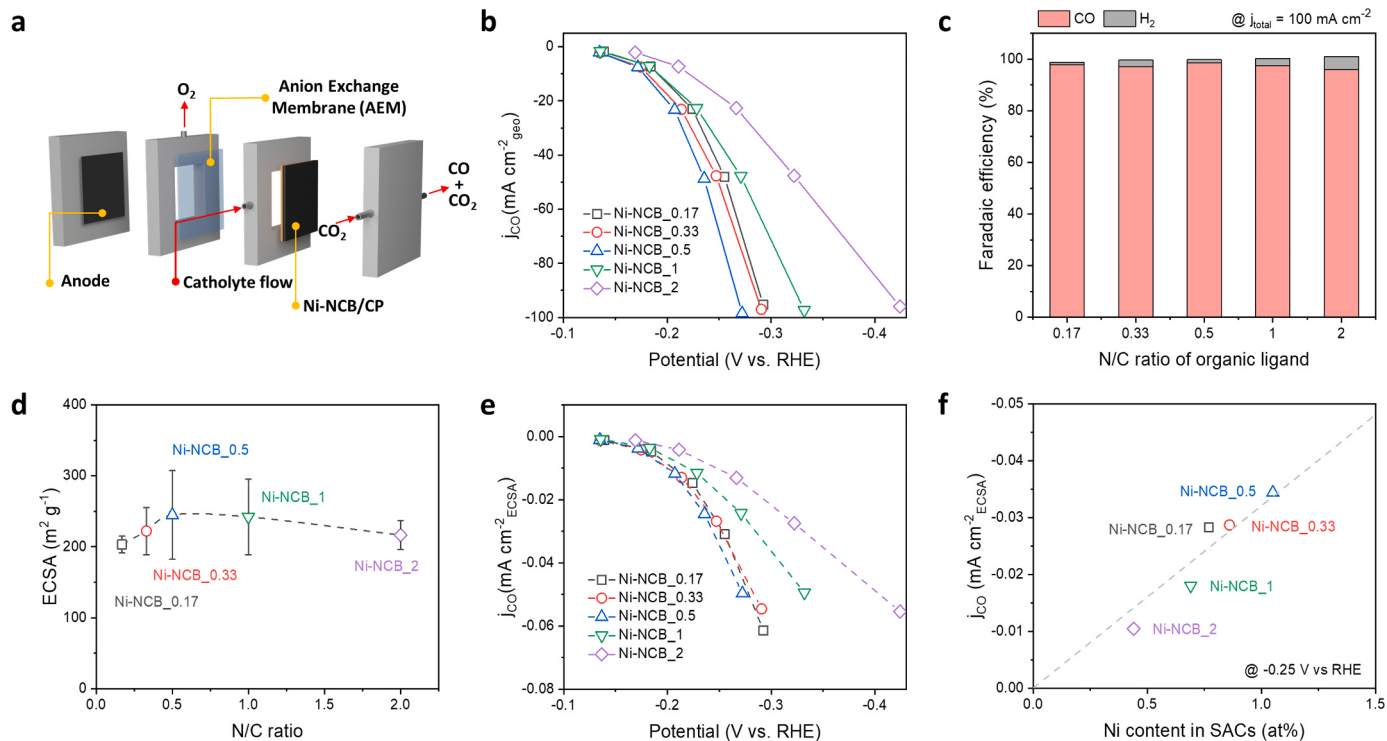


Fig. 5. Electrochemical results of Ni-NCB_N/Cs. (a) Scheme of the used gas diffusion electrode-based flow cell. (b) Linear sweep voltammetry (LSV) curves and (c) Faradaic efficiency of CO (FE_{CO}) produced from Ni-NCB_N/Cs at a total current density of 100 mA cm⁻². (d) Electrochemical surface area (ECSA) and (e) ECSA-normalized CO partial current densities (j_{CO}) of Ni-NCB_N/Cs. (f) Relationship between ECSA-normalized j_{CO} values and Ni contents of Ni-NCB_N/Cs. When error bars are presented, data are represented as mean \pm standard deviation of at least 3 individual experiments.

retain abundant exposed active sites for developing highly efficient s for CO₂RR.

The reaction kinetics of the CO₂RRs of all Ni-NCB_N/Cs were determined based on their Tafel slopes (Fig. S19d), which were in the following order: Ni-NCB_0.5 (69 mV decade⁻¹) < Ni-NCB_0.33 (76 mV decade⁻¹) < Ni-NCB_0.17 (77 mV decade⁻¹) < Ni-NCB_1 (81 mV decade⁻¹) < Ni-NCB_2 (93 mV decade⁻¹). This suggests that electrocatalysts with abundant atomic active sites promote the electron transfer to CO₂ or the reaction intermediates. The electrochemical impedance (EIS) spectra of the Ni-NCB_N/Cs were obtained at constant potential to compare their charge transfer properties (Fig. S20a). To precisely evaluate the charge transfer resistance (R_{CT}) of ECSA, the geometrically measured R_{CT} values were normalized using their ECSA values (Fig. S20b). A higher amount of exposed atomic active sites leads to a lower R_{CT} , indicating easy electron transfer from the electrocatalyst on the electrode to the reactants. Hence, we assumed that, as the number of exposed active sites facilitating charge transfer increased, similar to the decrease in resistance with an increase in the cross-sectional area, the charge transfer resistance diminished (Fig. S20c). This trend is consistent with the ECSA-normalized j_{CO} -at% Ni content results (Fig. 5f).

To further optimize and scale up our synthesis, we further optimized the ratio of the Ni and N precursors using the organic ligand with the optimal N/C ratio (2-MeIm, N/C = 0.5) (Fig. S21). The optimal Ni:N precursor ratio (1:16) is significantly lower than that of the primary ratio (1:4). To understand the differences in the performances of the Ni-NCBs, we analyzed the chemical states of the elements, Ni contents, and surface areas of the Ni-NCB_1:# samples using XPS, ICP, and ECSA (Fig. S22–24). The surface (XPS) Ni content changed as the Ni:N precursor ratio changed. Therefore, the excellent CO₂RR performance of Ni-NCB_1:16 is attributed to the abundant Ni active sites on its surface due to its moderate precursor ratio (Fig. S23). Insufficient N precursors could lead to inadequate spacing between Ni ions, resulting in their aggregation during the annealing process [32]. Conversely, an excessive

quantity of SOLs might result in a thick carbon surface, hindering the exposure of the atomic active sites.

To further explore the impact of carbon black, we conducted ECSA and CO₂RR tests on Ni-NC (Fig. S25). The sample with an N/C ratio of 0.5 displayed the highest ECSA, highlighting the significant role of the N/C ratio (Fig. S25a). Regarding CO₂RR performance, Ni-NC exhibited a slightly lower FE_{CO} and a higher FE_{H2} compared to its counterparts containing carbon black (Fig. S25b–e). Additionally, the mass activity, indicative of Ni utilization, of Ni-NC with carbon black (Ni-NCB) was significantly higher than that of Ni-NC without carbon black (Fig. S25f). Consequently, using carbon black is advantageous as it enhances Ni utilization while maintaining the effects of the N/C ratio.

Additionally, to assess the effect of calcination temperature on synthesis, CO₂RR tests were performed on samples synthesized at 600 °C. Despite these samples may possess less uniform active sites at this lower temperature, indicated by higher FE_{H2} compared to those synthesized at 800 °C, their enhanced CO₂RR performance is linked to a higher number of atomic active sites, as evidenced in the analyses (Fig. 3d, Fig. S14b, Fig. S26).

Subsequently, we scaled up the synthesis of Ni-NCBs to a gram-scale under the optimized conditions (Fig. S27). The resultant Ni-NCBs showed well-defined Ni-N active sites with spontaneously formed Ni NPs (Fig. S28). Additionally, to assess the activity of the carbon-shell coated Ni NPs in the CO₂RR, we analyzed the Ni-NCBs after strong acid leaching (6 M HCl). The CO₂RR activity did not decrease significantly even after removing the majority of Ni NPs (Fig. S29), suggesting that the carbon-encapsulated Ni NPs do not participate the electro-reduction of CO₂ to CO. Therefore, controlling the number of atomic active sites in the SACs is a promising approach for the development of highly efficient electrocatalysts.

3.3. CO₂RR catalytic activity of the cell stack of the optimized Ni-NCB

A cell stack ($25 \text{ cm}^2 \times 4\text{-stack}$) of the optimized Ni-NCB_0.5 was constructed, where each unit cell consisted of Ni-NCB on carbon paper (Ni-NCB/CP), IrO₂/Pt/Ti-mesh, AEM, and a bipolar plate (Fig. 6a), and the CO₂RR activities of the unit cell and the cell stack were evaluated. The unit cell achieved a maximum total current of 15.0 A at a cell voltage of 3.29 V, while the cell stack achieved 10.0 A at a stack voltage of 13.05 V (Fig. 6b), which confirms its potential for industrial-scale production. High CO Faradaic efficiencies were observed for the unit cell (> 96.4 % at 500 mA cm^{-2}) and the cell stack (> 87.7 % at 400 mA cm^{-2}) (Fig. 6c). Additionally, the maximum CO partial current densities of the unit cell and the cell stack were 523.73 and $350.92 \text{ mA cm}^{-2}$, respectively, despite the utilization of a large-scale stack system (Fig. 6d). Consequently, high CO energy efficiencies (EE_{CO}) were observed for the unit cell (41.23 % at 500 mA cm^{-2}) and the cell stack (36.04 % at 400 mA cm^{-2}) (Fig. 6e). Moreover, a single-pass conversion (SPC) of 49.78 %, which is close to the theoretical maximum of 50 % for AEM-based CO₂ electrolysis, was obtained for the unit cell (Fig. 6f) [33]. This SPC result is a crucial indicator for the CO₂/CO separation, which is a key process in this CO₂ conversion

technology. The CO yield calculated based on the CO partial current density of the cell stack of our Ni-NCB was $\sim 0.44 \text{ kg}$ per day. Notably, the maximum CO yield was approximately three times higher than that (0.147 kg per day) of a previously reported single-atom catalyst in a 100 cm^2 electrolysis cell (Fig. S30) [5,17,34,35]. The long-term stability of the cell stacks was evaluated by conducting stability tests using 3- and 4-stack cells (Fig. 6g and S31). The CO selectivity of the Ni-NCB after 50 h of operation of both cell stacks exceeded 96.0 %, which confirms its long-term stability. Furthermore, HAADF-STEM and XPS analyses of the Ni-NCB after the stability test revealed the presence of Ni single-atom active sites on the catalyst surface (Fig. S32). These results confirm the high stability of our Ni-NCBs and highlight the broad applicability of our simple strategy for SAC synthesis.

4. Conclusion

In this study, we investigated the effect of controlling the N/C ratios of the organic ligands used in the synthesis of Ni-NCBs on their electrocatalytic activities. The N/C ratio affected the number of N defects in the support material and the presence of abundant atomic active sites in the Ni-NCBs. Organic ligands with high N/C ratios exhibited thermally

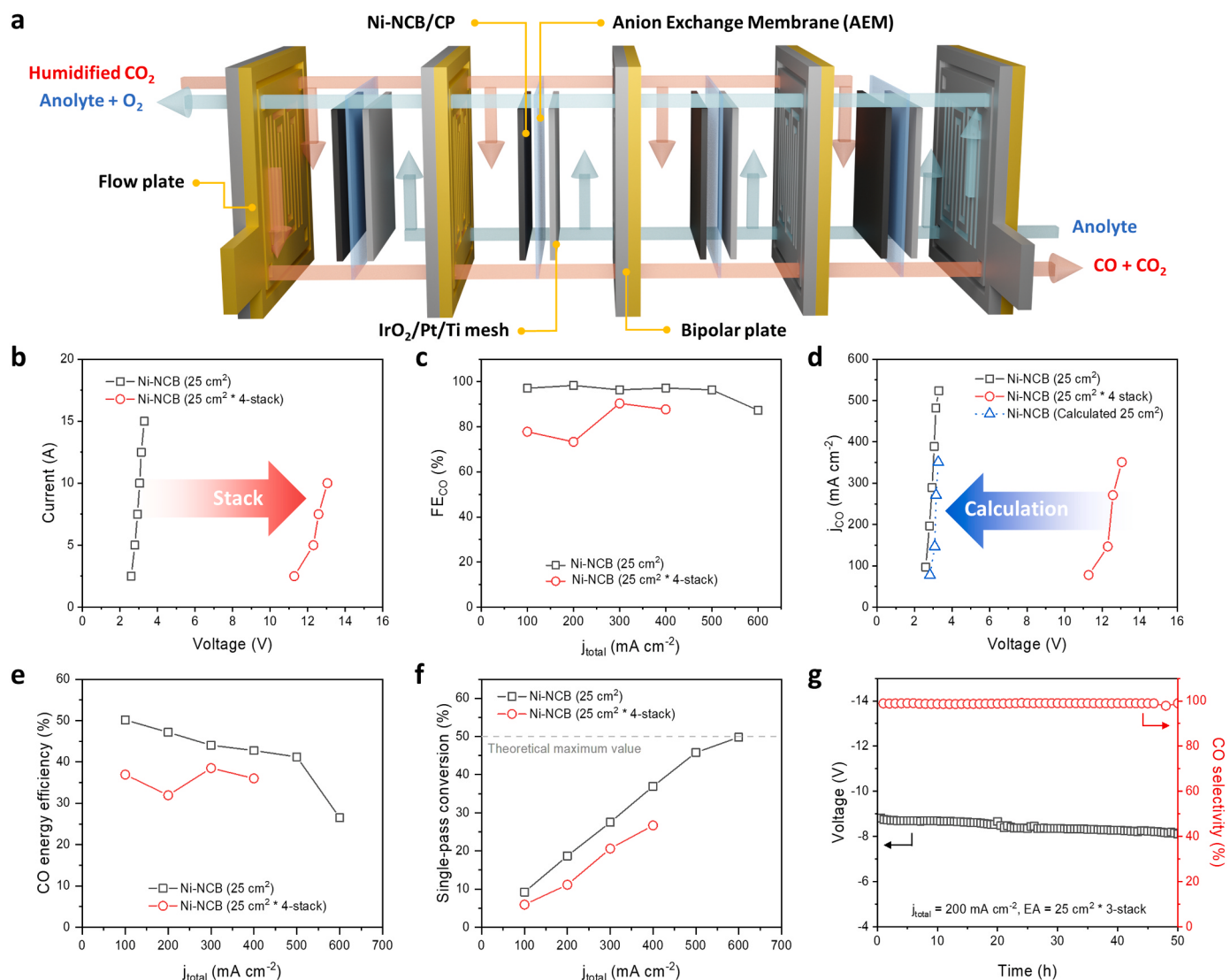


Fig. 6. Results of the electrolyzer stack constructed using the optimized Ni-NCB electrocatalyst. (a) Scheme of the 4-stack membrane assembly electrode system. (b) Current-V curves, (c) CO Faradaic efficiency, (d) j_{CO} -V curves, (e) CO energy efficiency, and (f) single-pass conversion of unit cell (25 cm^2) and cell stack ($25 \text{ cm}^2 \times 4\text{-stack}$) using the optimized Ni-NCB. (g) Stability results of the cell stack ($25 \text{ cm}^2 \times 3\text{-stack}$) using the optimized Ni-NCB.

unstable intermediate structures during the annealing process, resulting in Ni-NCBs with low N content. In contrast, the Ni-NCBs prepared using organic ligands with optimal N/C ratios demonstrated thermal stability, preserved their N content during calcination, and facilitated N-doping on the carbon support. The use of a suitable organic ligand achieved a N-rich surface, which anchored Ni atoms on the carbon support, leading to the formation of abundant Ni atomic active sites. The optimal Ni-NCB (N/C = 0.5, 1:# = 1:16) achieved excellent Faradaic efficiency for CO production (> 96.4 %) at a high current density (500 mA cm⁻², electrode area = 25 cm²), attributed to its abundance of atomic active sites. Moreover, to demonstrate the scalability of our strategy, we constructed a large-scale cell stack system with the Ni-NCBs (200 mA cm⁻², total electrode area = 100 cm²), which showed excellent electrocatalytic performance and stability over 50 h. This innovative synthesis strategy for SACs has potential for commercialization and can be extended to synthesize other industrial electrocatalysts.

CRediT authorship contribution statement

Jihun Oh: Writing – review & editing, Visualization, Supervision, Resources, Project administration, Funding acquisition, Conceptualization. **Jungwon Suh:** Investigation, Formal analysis, Data curation. **Min Gwan Ha:** Writing – review & editing, Resources, Methodology, Formal analysis, Data curation. **Hyeonuk Choi:** Writing – review & editing, Writing – original draft, Visualization, Validation, Methodology, Investigation, Formal analysis, Data curation, Conceptualization. **Jang Yong Lee:** Resources, Methodology, Investigation, Formal analysis. **Sun Eon Wang:** Validation, Methodology, Investigation. **Beomil Kim:** Resources, Methodology, Investigation. **Chulwan Lim:** Validation, Resources, Methodology, Formal analysis. **Hyung-Suk Oh:** Writing – review & editing, Supervision, Resources, Conceptualization.

Declaration of Competing Interest

The authors declare that they have no known competing financial interests or personal relationships that could have appeared to influence the work reported in this paper.

Data availability

The authors do not have permission to share data.

Acknowledgements

This work was supported by the National Research Foundation of Korea (NRF) grant funded by the Korea government (MSIT) (Nos. 2020M3H7A1096388, 2020M3H7A1098229, 2021R1A2C3007280, and 2021R1A5A1084921). This work was also supported by institutional program grants from the Korea Institute of Science and Technology (KIST), Republic of Korea.

Appendix A. Supporting information

Supplementary data associated with this article can be found in the online version at [doi:10.1016/j.apcatb.2024.124192](https://doi.org/10.1016/j.apcatb.2024.124192).

References

- [1] S. Ding, M.J. Hülse, J. Pérez-Ramírez, N. Yan, Transforming energy with single-atom catalysts, Joule 3 (2019) 2897–2929.
- [2] S. Mitchell, R. Qin, N. Zheng, J. Pérez-Ramírez, Nanoscale engineering of catalytic materials for sustainable technologies, Nat. Nanotechnol. 16 (2021) 129–139.
- [3] W. Song, C. Xiao, J. Ding, Z. Huang, X. Yang, T. Zhang, D. Mitlin, W. Hu, Review of carbon support coordination environments for single metal atom electrocatalysts (SACs), Adv. Mater. (2023) 2301477.
- [4] Y. Wang, H. Su, Y. He, L. Li, S. Zhu, H. Shen, P. Xie, X. Fu, G. Zhou, C. Feng, Advanced electrocatalysts with single-metal-atom active sites, Chem. Rev. 120 (2020) 12217–12314.
- [5] T. Zheng, K. Jiang, N. Ta, Y. Hu, J. Zeng, J. Liu, H. Wang, Large-scale and highly selective CO₂ electrocatalytic reduction on nickel single-atom catalyst, Joule 3 (2019) 265–278.
- [6] G.H. Jeong, Y.C. Tan, J.T. Song, G.-Y. Lee, H.J. Lee, J. Lim, H.Y. Jeong, S. Won, J. Oh, S.O. Kim, Synthetic multiscale design of nanostructured Ni single atom catalyst for superior CO₂ electroreduction, Chem. Eng. J. 426 (2021) 131063.
- [7] S.A. Abbas, J.T. Song, Y.C. Tan, K.M. Nam, J. Oh, K.-D. Jung, Synthesis of a nickel single-atom catalyst based on Ni-N_{4-x}C_x active sites for highly efficient CO₂ reduction utilizing a gas diffusion electrode, ACS Appl. Energy Mater. 3 (2020) 8739–8745.
- [8] H. Yang, L. Shang, Q. Zhang, R. Shi, G.I.N. Waterhouse, L. Gu, T. Zhang, A universal ligand mediated method for large scale synthesis of transition metal single atom catalysts, Nat. Commun. 10 (2019) 4585.
- [9] Z.-Y. Wu, P. Zhu, D.A. Cullen, Y. Hu, Q.-Q. Yan, S.-C. Shen, F.-Y. Chen, H. Yu, M. Shakouri, J.D. Arregui-Mena, A general synthesis of single atom catalysts with controllable atomic and mesoporous structures, Nat. Synth. 1 (2022) 658–667.
- [10] Y.S. Wei, M. Zhang, R. Zou, Q. Xu, Metal-organic framework-based catalysts with single metal sites, Chem. Rev. 120 (2020) 12089–12174.
- [11] H. Choi, D.-K. Lee, M.-K. Han, G. Janani, S. Surendran, J.H. Kim, J.K. Kim, H. Cho, U. Sim, Review—non-noble metal-based single-atom catalysts for efficient electrochemical CO₂ reduction reaction, J. Electrochem. Soc. 167 (2020).
- [12] X.-F. Yang, A. Wang, B. Qiao, J.U.N. Li, J. Liu, T. Zhang, Single-atom catalysts: a new frontier in heterogeneous catalysis, Acc. Chem. Res. 46 (2013) 1740–1748.
- [13] L. Han, H. Cheng, W. Liu, H. Li, P. Ou, R. Lin, H.-T. Wang, C.-W. Pao, A.R. Head, C.-H. Wang, A single-atom library for guided monometallic and concentration-complex multimetallic designs, Nat. Mater. 21 (2022) 681–688.
- [14] H.-Y. Zhuo, X. Zhang, J.-X. Liang, Q. Yu, H. Xiao, J. Li, Theoretical understandings of graphene-based metal single-atom catalysts: stability and catalytic performance, Chem. Rev. 120 (2020) 12315–12341.
- [15] D. Deng, X. Chen, L. Yu, X. Wu, Q. Liu, Y. Liu, H. Yang, H. Tian, Y. Hu, P. Du, A single iron site confined in a graphene matrix for the catalytic oxidation of benzene at room temperature, Sci. Adv. 1 (2015) e1500462.
- [16] X. Hai, S. Xi, S. Mitchell, K. Harrath, H. Xu, D.F. Akl, D. Kong, J. Li, Z. Li, T. Sun, Scalable two-step annealing method for preparing ultra-high-density single-atom catalyst libraries, Nat. Nanotechnol. 17 (2022) 174–181.
- [17] C. Lim, W.H. Lee, J.H. Won, Y.J. Ko, S. Kim, B.K. Min, K.Y. Lee, W.S. Jung, H.S. Oh, Enhancement of catalytic activity and selectivity for the gaseous electroreduction of CO₂ to CO: guidelines for the selection of carbon supports, Adv. Sustain. Syst. 5 (2021) 2100216.
- [18] M.J. Jang, S.H. Yang, M.G. Park, J. Jeong, M.S. Cha, S.-H. Shin, K.H. Lee, Z. Bai, Z. Chen, J.Y. Lee, Efficient and durable anion exchange membrane water electrolysis for a commercially available electrolyzer stack using alkaline electrolyte, ACS Energy Lett. 7 (2022) 2576–2583.
- [19] Y. Zhan, H. Zeng, F. Xie, H. Zhang, W. Zhang, Y. Jin, Y. Zhang, J. Chen, H. Meng, Templated growth of Fe/N/C catalyst on hierarchically porous carbon for oxygen reduction reaction in proton exchange membrane fuel cells, J. Power Sources 431 (2019) 31–39.
- [20] J.-Y. Wang, T. Ouyang, N. Li, T. Ma, Z.-Q. Liu, S. N co-doped carbon nanotube-encapsulated core-shell CoS₂/Co nanoparticles: efficient and stable bifunctional catalysts for overall water splitting, Sci. Bull. 63 (2018) 1130–1140.
- [21] C. Zhao, Y. Wang, Z. Li, W. Chen, Q. Xu, D. He, D. Xi, Q. Zhang, T. Yuan, Y. Qu, J. Yang, F. Zhou, Z. Yang, X. Wang, J. Wang, J. Luo, Y. Li, H. Duan, Y. Wu, Y. Li, Solid-diffusion synthesis of single-atom catalysts directly from bulk metal for efficient CO₂ reduction, Joule 3 (2019) 584–594.
- [22] J.P. Gore, A. Sane, Flame synthesis of carbon nanotubes, Carbon Nanotub.-Synth. Charact. Appl. 1 (2011) 16801.
- [23] S. Liang, Q. Jiang, Q. Wang, Y. Liu, Revealing the real role of nickel decorated nitrogen-doped carbon catalysts for electrochemical reduction of CO₂ to CO, Adv. Energy Mater. 11 (2021) 2101477.
- [24] K.P. Kuhl, T. Hatsukade, E.R. Cave, D.N. Abram, J. Kibsgaard, T.F. Jaramillo, Electrocatalytic conversion of carbon dioxide to methane and methanol on transition metal surfaces, J. Am. Chem. Soc. 136 (2014) 14107–14113.
- [25] J.-B. Wu, M.-L. Lin, X. Cong, H.-N. Liu, P.-H. Tan, Raman spectroscopy of graphene-based materials and its applications in related devices, Chem. Soc. Rev. 47 (2018) 1822–1873.
- [26] Z. Xiong, B. Sun, H. Zou, R. Wang, Q. Fang, Z. Zhang, S. Qiu, Amorphous-to-crystalline transformation: general synthesis of hollow structured covalent organic frameworks with high crystallinity, J. Am. Chem. Soc. 144 (2022) 6583–6593.
- [27] Y.N. Gong, L. Jiao, Y. Qian, C.Y. Pan, L. Zheng, X. Cai, B. Liu, S.H. Yu, H.L. Jiang, Regulating the coordination environment of MOF-templated single-atom nickel electrocatalysts for boosting CO₂ reduction, Angew. Chem. 132 (2020) 2727–2731.
- [28] H. Fei, J. Dong, Y. Feng, C.S. Allen, C. Wan, B. Voloskiy, M. Li, Z. Zhao, Y. Wang, H. Sun, General synthesis and definitive structural identification of MN₄C₄ single-atom catalysts with tunable electrocatalytic activities, Nat. Catal. 1 (2018) 63–72.
- [29] S. Thapa, R. Paudel, M.D. Blanchet, P.T. Geperline, R.B. Comes, Probing surfaces and interfaces in complex oxide films via in situ X-ray photoelectron spectroscopy, J. Mater. Res. 36 (2021) 26–51.
- [30] V. Giulimondi, S. Mitchell, J. Pérez-Ramírez, Challenges and opportunities in engineering the electronic structure of single-atom catalysts, ACS Catal. 13 (2023) 2981–2997.
- [31] W.-J. Ong, L.-L. Tan, Y.H. Ng, S.-T. Yong, S.-P. Chai, Graphitic carbon nitride (g-C₃N₄)-based photocatalysts for artificial photosynthesis and environmental remediation: are we a step closer to achieving sustainability? Chem. Rev. 116 (2016) 7159–7329.

- [32] C. Xia, Y. Qiu, Y. Xia, P. Zhu, G. King, X. Zhang, Z. Wu, J.Y. Kim, D.A. Cullen, D. Zheng, General synthesis of single-atom catalysts with high metal loading using graphene quantum dots, *Nat. Chem.* 13 (2021) 887–894.
- [33] C.P. O'Brien, R.K. Miao, S. Liu, Y. Xu, G. Lee, A. Robb, J.E. Huang, K. Xie, K. Bertens, C.M. Gabardo, J.P. Edwards, C.-T. Dinh, E.H. Sargent, D. Sinton, Single pass CO₂ conversion exceeding 85% in the electrosynthesis of multicarbon products via local CO₂ regeneration, *ACS Energy Lett.* 6 (2021) 2952–2959.
- [34] B. Endrődi, E. Kecsenovity, A. Samu, F. Darvas, R.V. Jones, V. Török, A. Danyi, C. Janáky, Multilayer electrolyzer stack converts carbon dioxide to gas products at high pressure with high efficiency, *ACS Energy Lett.* 4 (2019) 1770–1777.
- [35] B. Endrődi, A. Samu, E. Kecsenovity, T. Halmágyi, D. Seböök, C. Janáky, Operando cathode activation with alkali metal cations for high current density operation of water-fed zero-gap carbon dioxide electrolyzers, *Nat. Energy* 6 (2021) 439–448.